Nano Energy 68 (2020) 104311

Contents lists available at ScienceDirect

Nano Energy

journal homepage: http://www.elsevier.com/locate/nanoen

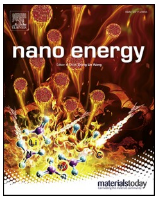

Full paper

Collective behaviors mediated multifunctional black sand aggregate towards environmentally adaptive solar-to-thermal purified water harvesting

Feng Ni[a,b], Peng Xiao[a,b,*], Nianxiang Qiu[c], Chang Zhang[a], Yun Liang[a,b], Jincui Gu[a,b], Junyuan Xia[a,b], Zhixiang Zeng[a,b], Liping Wang[a,b], Qunji Xue[a,b], Tao Chen[a,b,**]

[a] *Key Laboratory of Marine Materials and Related Technologies, Zhejiang Key Laboratory of Marine Materials and Protective Technologies, Ningbo Institute of Material Technology and Engineering, Chinese Academy of Sciences, Zhongguan West Road 1219, 315201, Ningbo, China*

[b] *School of Chemical Sciences, University of Chinese Academy of Science, Beijing, 100049, China*

[c] *Engineering Laboratory of Advanced Energy Materials, Ningbo Institute of Material Technology and Engineering, Chinese Academy of Sciences, Zhongguan West Road 1219, 315201, Ningbo, China*

ARTICLE INFO

Keywords:
Collective behaviors
Sand aggregate
Solar energy
Multifunction
Purified water collection under changeable environments

ABSTRACT

As a renewable and efficient technology, interfacial solar heating has emerged as a new and promising avenue for treating undrinkable water to clean one via a variety of well-designed solar absorbers. However, it is still urgent to develop an accessible material system in a simple, low-cost and effective way to easily tackle water shortage. Inspired by natural sand with highly important role in purifying water during the natural recycling, in this work, we demonstrate a concept of an all-round black sand aggregate with specific collective behaviors for environmentally adaptable clean water collection from seawater, polluted water and even atmospheric moisture. To endow the raw sand desirable photo-thermal features, polydopamine and Cl^--doped polypyyrole are successively modified onto the sand surface for a stable structure. Owing to the specific aggregative structure of the black sands, a self-channelled device combined adjustable 2D/3D solar-driven evaporation can be readily achieved, and yield a high evaporation performance (1.43 kg m^{-2} h^{-1}) in comparison with other reported naturally derived materials. Notably, the black sand aggregate could handle with oil-contained polluted water (P-WA) to guarantee high-efficient and sustainable water purification. Furthermore, even if in some draughty areas or deserts, the collective black sands could also extract water from air by absorbing atmospheric moisture and sequentially realizing an *in situ* water evaporation by heat location. The successful demonstration of multifunctional black sand aggregate may provide a new avenue for purified water collection under changeable environments.

1. Introduction

The shortage of clean water is a major public health problem, which severely affects the living quality of human beings in extended regions, including coastal cities, developed industrial districts and droughty areas/deserts [1–5]. As a renewable and sustainable resource, sunlight has become a predominant and promising alternative for treating vast saline or polluted water into clean one [6,7]. Over the past few years, sunlight-driven interfacial evaporation that directly converts solar to thermal energy has bloomed due to its easily accessible and high-efficient properties in the field of water purification, desalination or sterilization [8–11]. Currently, extensive efforts have been dedicated to construct diverse natural/synthetic-derived solar absorbers to realize seawater evaporation with specific features, such as high evaporation ratio [12,13], unique salt-rejection performance [14–16], additional function integration of power generation [17–19], pollutant detection [20], and photocatalysis [9,21], etc.

Up to now, most research has focused on the desalination of seawater, it is highly important to extend the applicable area of solar-driven water purification to adapt to multiple environments, which

---

* Corresponding author. Key Laboratory of Marine Materials and Related Technologies, Zhejiang Key Laboratory of Marine Materials and Protective Technologies, Ningbo Institute of Material Technology and Engineering, Chinese Academy of Sciences, Zhongguan West Road 1219, 315201, Ningbo, China.

** Corresponding author. Key Laboratory of Marine Materials and Related Technologies, Zhejiang Key Laboratory of Marine Materials and Protective Technologies, Ningbo Institute of Material Technology and Engineering, Chinese Academy of Sciences, Zhongguan West Road 1219, 315201, Ningbo, China.

E-mail addresses: xiaopeng@nimte.ac.cn (P. Xiao), tao.chen@nimte.ac.cn (T. Chen).

https://doi.org/10.1016/j.nanoen.2019.104311
Received 28 September 2019; Received in revised form 8 November 2019; Accepted 17 November 2019

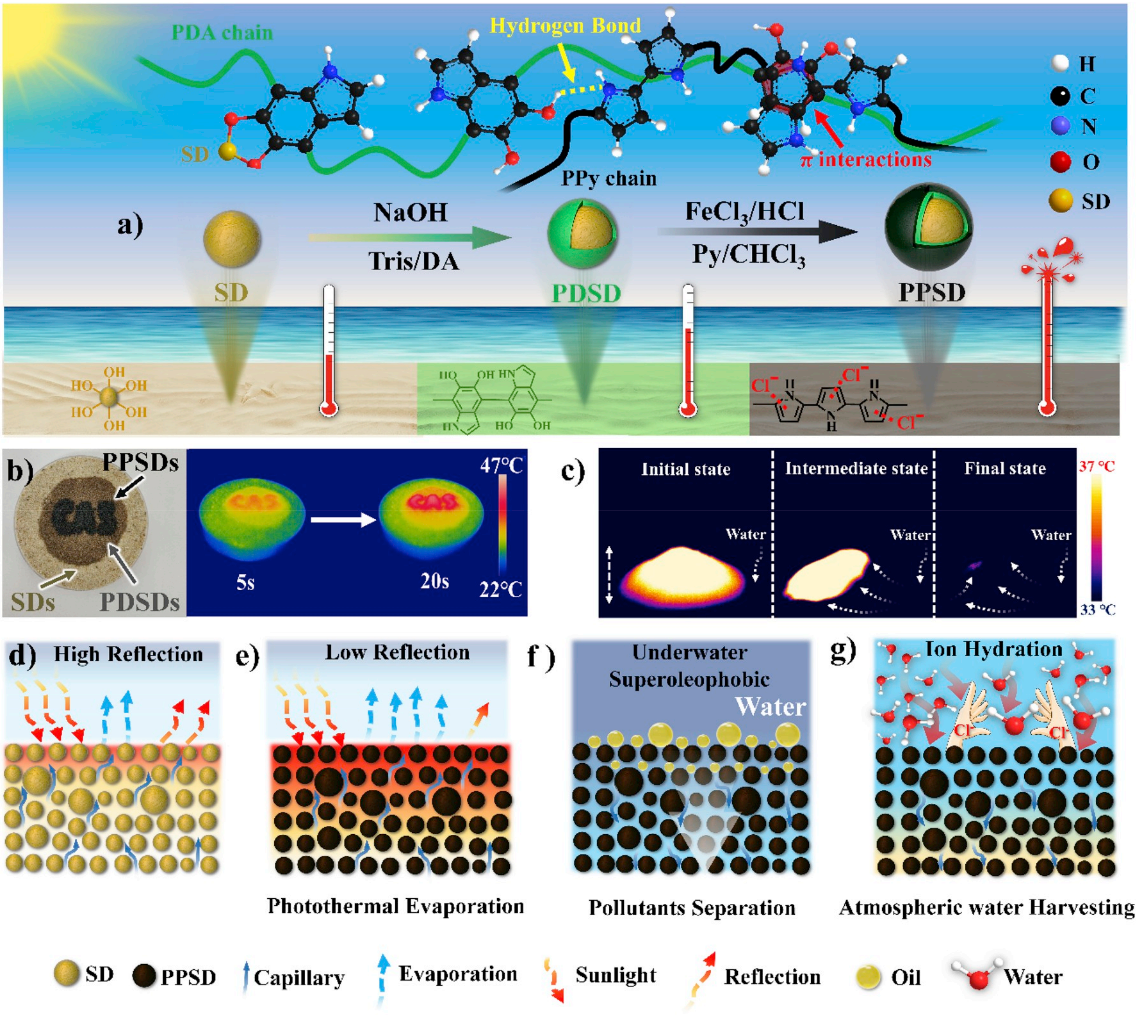

Fig. 1. a) Schematic fabrication of PPSDs. The upper insert sketches reveal that interactions between different components in PPSDs, and the lower inserts display ingredients of materials on the outer surfaces. b) The left part is digital photography of sands (SDs), PDA/sands (PDSDs), and PPSDs, respectively. The outer ring refers to SDs, and PDSDs form the inner ring, and the words "CAS" consist of PPSDs. The right part are IR thermal images of sand aggregates after five and 20 s under one sun illumination. c) IR images of PPSD aggregate, which prove that the achieved PPSDs has a capacity of water pumping because of its self-organized pores inside. The high-temperature region represents dry PPSDs, and their temperature will drop when wetted. The two-way dotted arrow in initial state indicates that the height of the PPSDs is ~40 mm. One-way arrows represent the direction of water flow. d) The natural sands show relatively high reflection, resulting in a lower absorption of sunlight. e) After sequential modification of photothermal polymer, a low reflection and high solar absorption can be observed, which wad favourable for photothermal evaporation. f) The achieved PPSDs aggregate can realize pollutants separation. g) The resulted PPSDs can achieve atmospheric water harvesting.

aims to further broaden access to clean water in wide remote or droughty regions. More recently, spontaneous atmospheric moisture harvesting towards smart and solar heating clean water collection enabled by saturation salt solution or salt-doped hybrid has aroused renewed interest, providing an attractive pathway to relieve the water scarcity in droughty inland regions [22,23]. However, it is still challenging for realization of environmentally changeable water collection within one material system in a simple, scalable and low-cost way.

Natural sea sand (SD), mainly composed of silicon dioxide, is not suitable for structural materials in the infrastructure filed is massively acquired and very cheap. However, it also can be further modified to a class of useful materials. The abundant hydroxyl groups on its surface endow the sand particle with high surface energy for intrinsic water attraction [24]. Moreover, the collective behaviors of sand particles can result in self-organized pores in micron scale and configurable shapes. Such porous structures can further generate desirable capillary force to draw water from bottom to the top layer, which can function as effective water-pumping channels. Hence, compared with the synthetic porous structures or modified porous natural materials, the locally sourced sand in abundance is considered as a good alternative to construct self-channelled functional material with simple and large-scale preparation. In this work, a multifunctional photothermal sand composed of polydopamine (PDA) and Cl^--doped-polypyrrole (PPy) was rationally designed in a facile, extensive and inexpensive way, which can highly adapt to diverse environments for clean water collection. In our system, the PDA anchored on sand surface can both function as the infrared absorber and effective binder to bridge the gap between sand and PPy with π interactions and hydrogen bonds for a stable black sand. The collective behaviors enabled the achieved black sand aggregate effective self-channelled and photo-thermal property for 2D/3D solar-driven interfacial water purification, and the 3D aggregate demonstrated a high purification performance (1.43 kg m^{-2} h^{-1} under one sun illumination) compared with other state-of-the-art naturally derived materials. When the water resource suffers from pollution from cities and industrial areas, to achieve a high-efficient and sustainable water purification, the close-packed micro-scale pores of the collective black sand particles allow further treatment of polluted water through efficient separation of water/oil hybrids for subsequent locating heating evaporation. Specifically, owing to synergistic effect of the introduction of $FeCl_3$ and capillary force mediated by inner channels in the sand system,

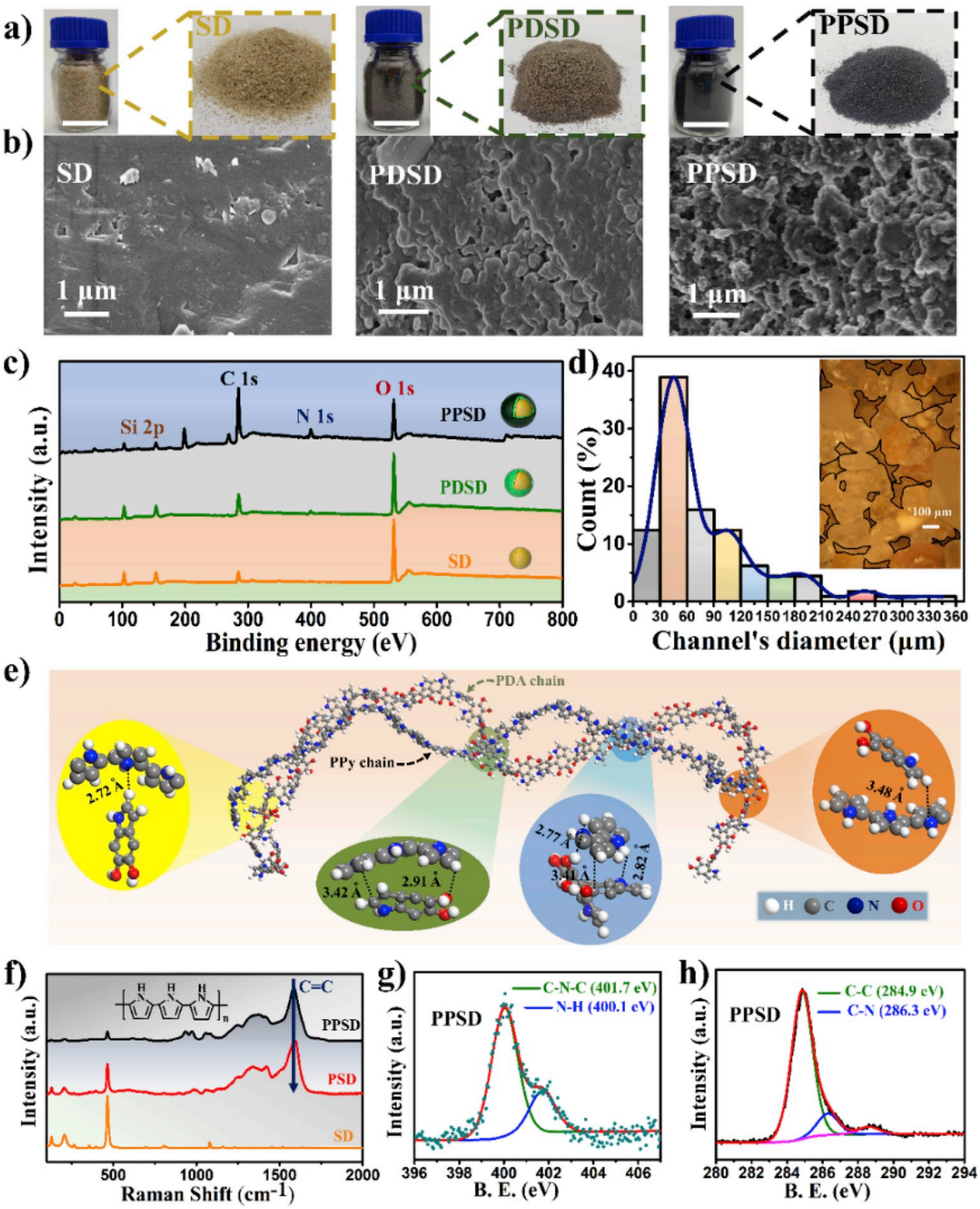

Fig. 2. a) Digital photographs show pure SD, PDSD, and PPSD, respectively. The color gradually deepens as successive modification. The scale bar in the photographs is 5 cm. b) SEM images of surface of SD, PDSD and PPSD, respectively. c) XPS survey spectra of SD, PDSD and PPSD, respectively. d) Distribution of diameter of self-organized pores on the cross-section in collective SDs aggregate (marked with a black box in the insert image). e) Molecular simulation results of interactions between PPy and PDA chains in PPSDs. f) Raman spectrum of PPSD, PSD, SD, respectively. g, h) High-resolution XPS spectrum for N and C of PPSD.

it can even absorb atmospheric moisture and further realize a self-sustaining solar steam generation in some droughty areas or deserts. Therefore, the concept of multifunctional black sand aggregate has provided a new pathway to realize an environmentally adaptive purified water collection in changeable circumstance.

2. Results and discussions

The photothermal black sand was directly obtained from natural sand via a scalable solution-based method, which can mainly be divided to two steps as revealed in Fig. 1a. Generally, the sodium hydroxide (NaOH) aqueous solution was firstly employed to treat the natural sand to fabricate a rough surface, ensuring subsequent stable polymers anchor on its surface (Fig. S1). To endow the sand particles desirable light absorption, polydopamine (PDA) was firstly modified onto the sand surface to bind the photothermal PPy polymer via multiple π interactions and hydrogen bonds. Finally, the stable black sand of polypyrrole/polydopamine/sand (PPSD) was readily achieved. Note that the two critical features have played significant roles in realizing efficient interfacial solar-driven water evaporation, including solar-to-thermal conversion and water pumping. Since the successive introduction of photothermal polymers, the capability of solar-to-thermal conversion of the black sand aggregate can experience a remarkable improvement process. To clearly demonstrate the temperature difference among these samples, a specific pattern was designed in Fig. 1b. When one sun intensity was applied on the pattern surface, the surface temperature of the SDs and PDSDs can reach to 30.5 °C and 35.9 °C, respectively. Furthermore, with the modification of photothermal PPy polymer, the temperature of the achieved PPSDs can rise to 43.4 °C in just 20 s under 1 sun illumination (Fig. 1b). Moreover, the capability of water pumping is also considered as an important property for the light absorbers. In our system, similar to the raw natural sand, the resulted PPSDs aggregate still maintained excellent water-pumping ability, in which the water molecules could be easily transported to a height of 40 mm (Fig. 1c and S2).

Despite the fact that the raw sand aggregate containing water molecules can also achieve a higher evaporation rate than that of the bulk water, the high reflection and low absorption of the unmodified sand severely limit the utilization efficiency of the solar energy (Fig. 1d and S3). For the PPSDs system, the introduction of functional photothermal

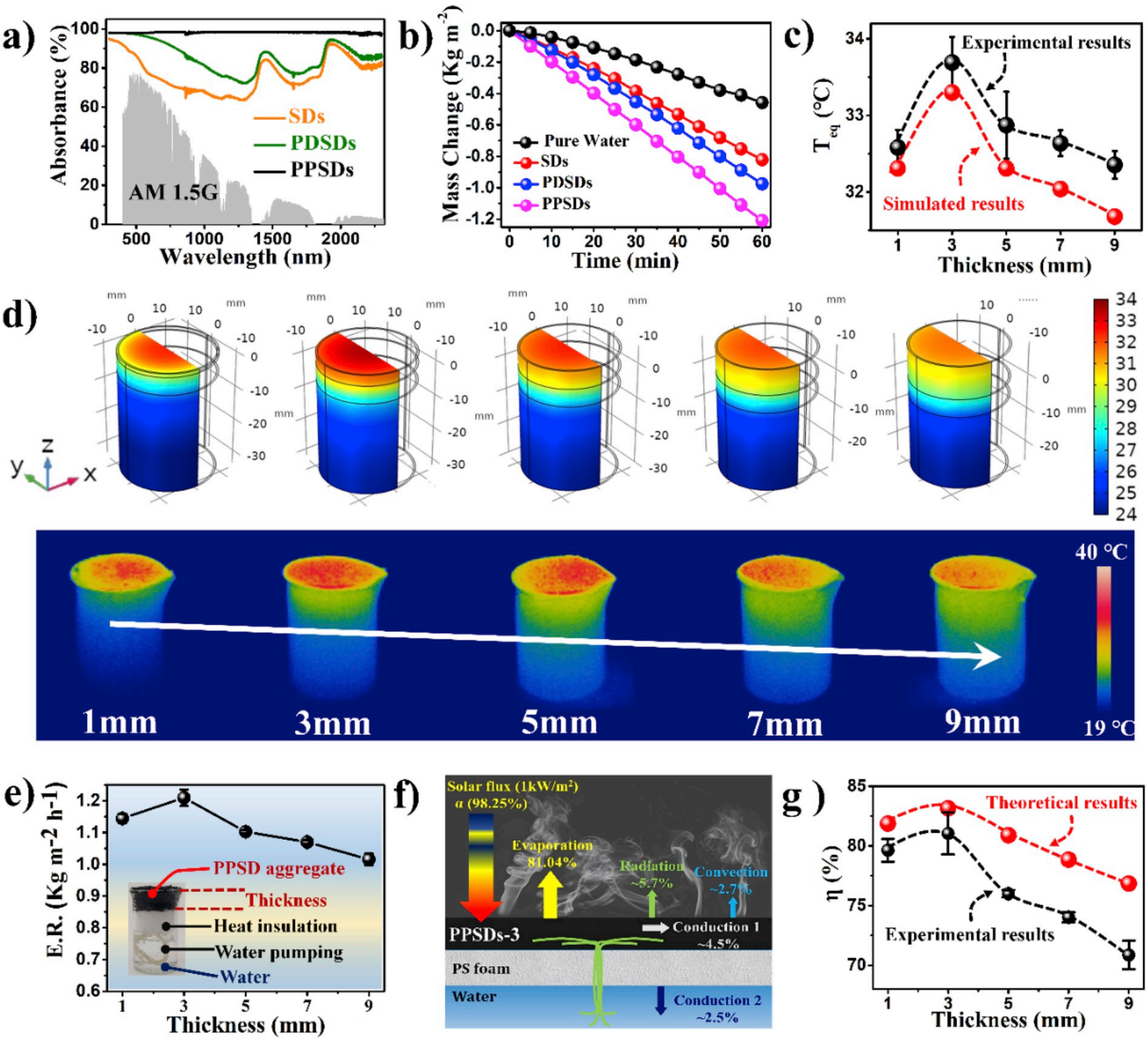

Fig. 3. a) The UV–vis-IR absorption spectrum of SDs, PDSDs, PPSDs in the wavelength range of 400 to 2300 nm, respectively, and comparison with the standard AM 1.5G spectrum filter (gray). The thickness of all samples was 3 mm in this experiment. b) Mass change of SDs, PDSDs, and PPSDs and pure water under one sun illustration over time. c) T_{eq} of PPSDs with various thickness from 1 to 9 mm by experiment and simulation under one sun. d) Temperature distribution of PPSDs when equilibrated with various thickness from 1 mm to 9 mm by COMSOL simulation (upper part) and experiment (lower part) under one sun. e) Evaporation rate (E. R.) of PPSDs with various thickness from 1 mm to 9 mm. f) Schematic figure of heat loss model of PPSDs-3. g) Theoretical results calculated from heat loss model of PPSDs show same trend as experimental results of solar-to-thermal conversion efficiency (η).

polymers can effectively absorb the illuminated sunlight and remarkably accelerate the interfacial seawater evaporation process with high efficiency (Fig. 1e). In addition, benefiting from the collective behaviors of PPSDs, the resulted black sand aggregate can be endowed with excellent under-water superoleophobic property, which can function as the oil-water emulsion separator to prevent the potential contamination from industrial and/or domestic polluted water for further interfacial evaporation (Fig. 1f). Furthermore, the exposed Cl^- inside the black sand aggregate can even absorb atmospheric moisture induced by synergism of ion hydration effect and capillary force, in which the captured water can be further released by localized solar heating in some droughty areas or deserts (Fig. 1g).

Macroscopically, the original SD appeared yellow with a certain cluster. After modification of PDA, the color of sand sample turned dark green. Finally, the color changed to black when PPy was anchored on the outer surface of PDA-decorated SDs (PDSDs) (Fig. 2a). Similarly, before and after modification, the surface of the SD also changed dramatically on a microscopic scale, illustrating in Fig. 2b and S4. To clarify element changes on the surface of sand samples, X-ray photoelectron spectroscopy (XPS) analysis was conducted. As shown in Fig. 2c and S5, SD had the highest Si peak among three samples and almost no N signal was observed. Compared with the raw SD, remarkable N peak appeared in the spectra of the other two samples, in which the intensity of N peak represented an increase process. Moreover, the intensity of O peak slightly decreased after coating PPy, which derived from less O-contained functional group of PPy than PDA. Furthermore, it was noted that there were abundant self-organized pores of ~45 μm in diameter on the cross section of the sand aggregate (Fig. 2d and S6). As a result, these micron-scale pores enabled collective sand an excellent water-wicking ability and this capillary effect could be effectively maintained after chemical modification (Fig. S7).

Due to the excellent adhesive property of PDA, it was introduced onto the surface of raw SD to stably anchor the hydrophobic PPy polymer. For comparison, polypyrrole/sand (PSD) was prepared by repeating the entire procedure as described above except for the self-polymerization of DA. As displayed in Fig. S8, the PPSD sample demonstrated a more stable state than that of PSD. The results illustrated that PDA can effectively bridge a robust binder between hydrophilic SD

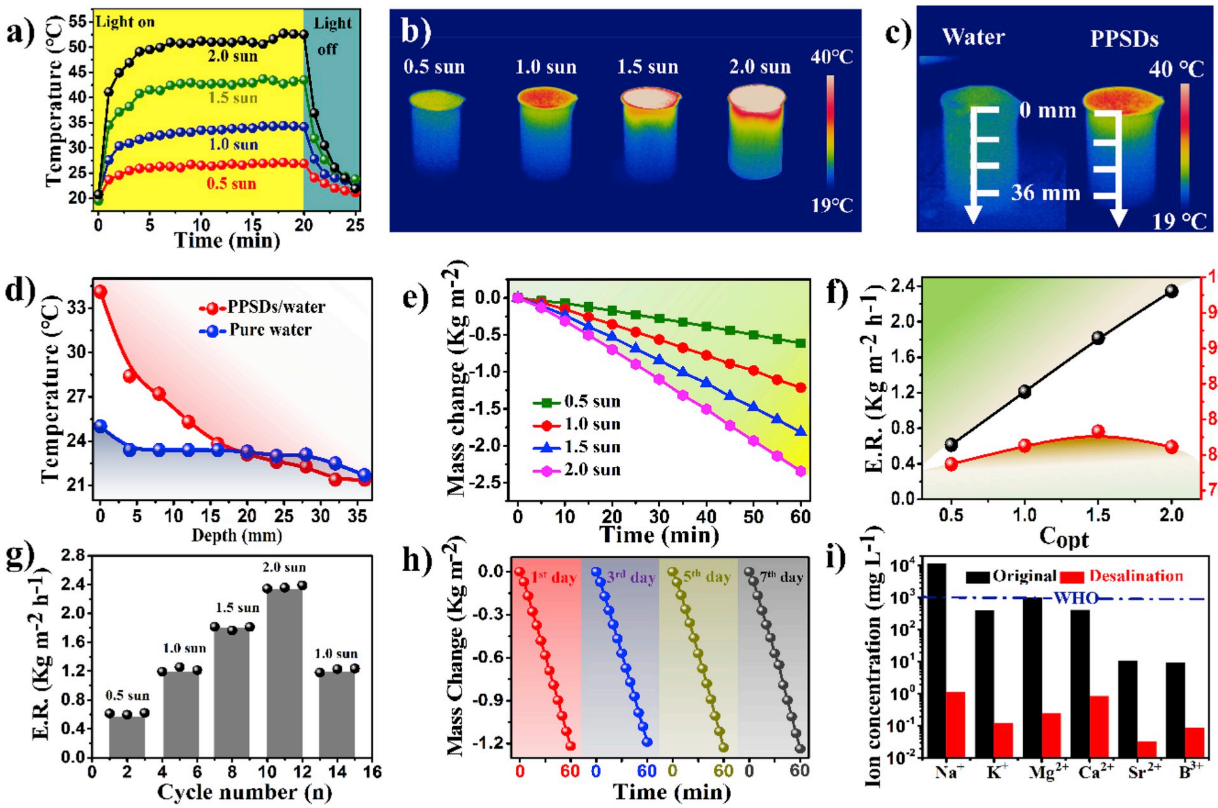

Fig. 4. a) The temperature changes as a function of irradiation time of PPSDs-3 under 0.5–2.0 sun illumination on and off. b) IR thermal images of PPSDs-3 when equilibrated under 0.5–2.0 sun. c) Temperature distribution in the vertical direction of PPSDs-3 and pure water under 1.0 sun. d) Temperature profiles of the white marked lines in the c) when temperatures were equilibrated under one sun irradiation. e) The mass change of water with PPSDs-3 over time at different solar power densities increasing from 0.5 to 2.0 sun. f) Evaporation rate (E.R.) and solar-to-thermal conversion efficiency (η) of PPSDs-3 under different optical concentration (C_{opt}) varying from 0.5 to 2.0 sun. g) The measured evaporation cycle performance of PPSDs-3 under different solar concentrations. h) The evaporation durability of PPSDs-3 under one-sun irradiation. i) The measured concentration of four primary ions before and after desalination with PPSDs-3. The blue dashed lines represent the WHO standard for drinking water.

and hydrophobic PPy. To further evidence the potential mechanism, a molecular simulation was conducted to simulate the interaction between PDA and PPy chains using Forcite plus module as implemented in Materials Studio software, which was explained in detail in **Section S3**. As shown in Fig. 2e, two molecular chains were not jointed flat as usual, but form a double-helix structure similar to the DNA molecule. Additionally, it can be found that the long-range Van der Waals interactions at twist point are critical for the stability of PPSD, which includes hydrogen bonds, π interactions (π-π stacking, π-H), etc. (shown in inserts of Fig. 2e). As expected, compared to PSD, the PPSD has a better stability benefiting from the above-mentioned interactions. In order to further verify theoretical analysis, Raman spectra and high-resolution XPS spectra were conducted. Fig. 2f and S9 demonstrated that the characteristic Raman peak of C═C in pyrrole ring of PPSD had a slightly downshifted frequency (1588 cm^{-1}) compared with PSD (1593 cm^{-1}), which was consistent with the electronic effects of the π interactions between PDA and PPy chains. The result confirmed that there were more π interactions in the PPSD [25–27]. In addition, the high-resolution XPS spectra was also measured to verify hydrogen bonds and π interactions between PDA and PPy chains. As shown in Fig. 2g and S10a, owing to the existence of more hydrogen bonds between PDA and PPy chains, the N–H peak of PPSD had a stronger binding energy in comparison with PSD. Additionally, the C–C peak of PPSD slightly upshifted from 284.6 eV for PSD to 284.9 eV for PPSD, which resulted from π interactions between PDA and PPy chains (Fig. 2f and S10b) [28]. As stated above, due to the introduction of PDA in PPSD, PPy demonstrated a stronger adhesion to the outer surface of SD, which is beneficial for its further application.

The ability to absorb light is a key factor in determining the performance of solar-to-thermal conversion of materials [29]. From the UV–vis-IR absorption spectrum in Fig. 3a, it can be observed that SDs initially has a certain light absorption, but the sequential modification significantly enhanced the light absorption of sand samples. It should be pointed out that 3 mm-PPSDs (PPSDs-3) has 98.25% absorption of total solar energy (weighted under AM 1.5G) in the wavelengths from 400 to 2500 nm, corresponding to the characteristic broad-band absorption of modified materials (PPy and PDA) and enhanced light scattering of the rough surface of the achieved PPSD aggregate. The △T refers to the difference between the initial temperature and equilibrated temperature (T_{eq}) of solar absorber under sun illumination, which can reflect the ability of photothermal conversion [30]. As reflected in Fig. S11, the △T of solar absorber of PPSDs was six times more than that of water, which could reach ~13 °C under one sun irradiation. Consequently, PPSDs exhibited the maximum evaporation rate (E.R.), which was 2.6 times larger than pure water (0.46 kg m^{-2} h^{-1}) (Fig. 3b). Note that in the evaporation device (illustrated in Fig. S12) in our system, the thickness of the solar absorber is a one of major factor affecting its evaporation performance. In order to evaluate the influence of thickness of PPSDs for evaporation performance, T_{eq} of PPSDs with different thickness were measured using the IR images. As shown in Fig. 3c, when the thickness of PPSDs rised from 1 mm to 9 mm, T_{eq} initially increased and then decreased. In addition, the experiment result was further simulated by COMSOL Multiphysics, which were highly coincided to the above-mentioned tendency (detailed discussion in **Section S4**). The IR images and simulated results were displayed in Fig. 3d, in which the maximum T_{eq} of PPSDs with the thickness of about 3 mm can reach up to 33.5 °C.

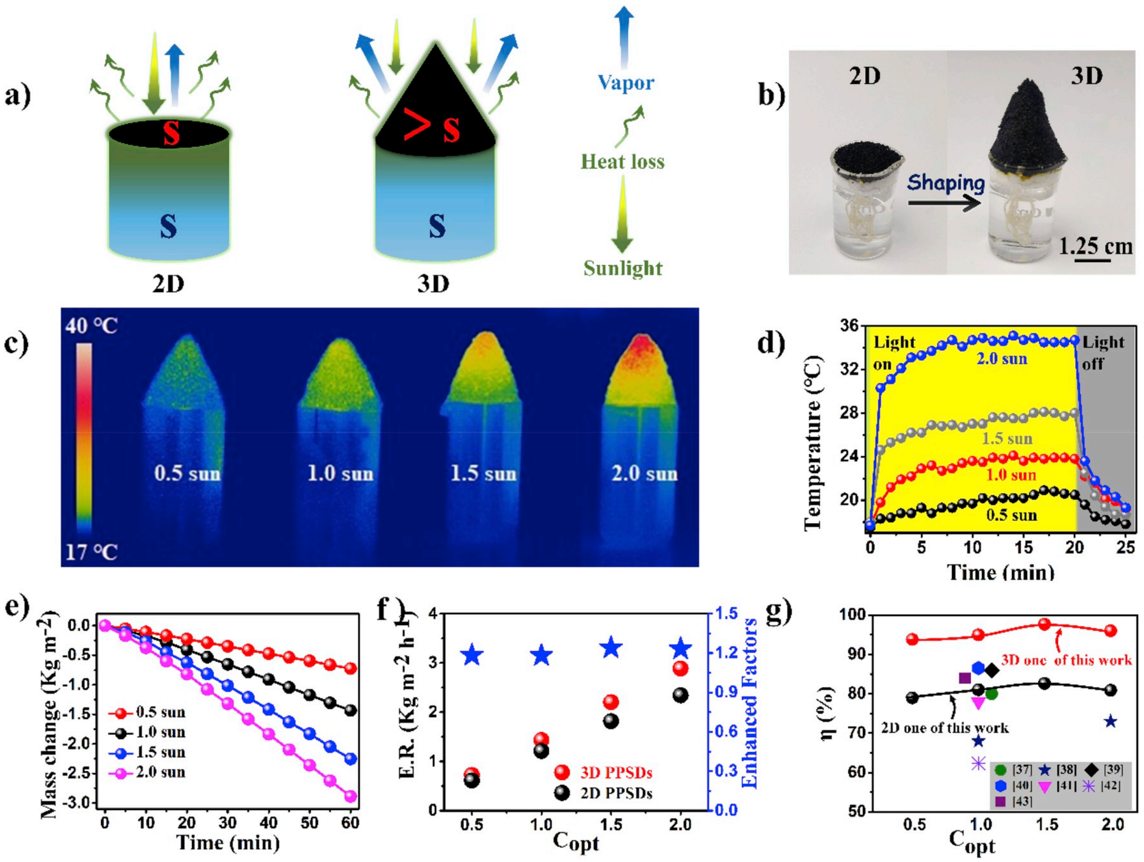

Fig. 5. a) Physical mechanism of enhanced evaporation performance of 3D PPSDs. Due to less heat loss and expanding evaporation area, 3D PPSDs demonstrated an improved evaporation performance compared to 2D one. The blue "S" is the projected area, and the red "S" represents effective area. b) The transformation from 2D PPSDs to 3D PPSDs by shaping, similar to making sand sculptures. c) The IR thermal images of 3D PPSD under the solar intensity of 0.5.1.0, 1.5, and 2.0 sun irradiation, respectively. d) The measured temperatures change as a function of irradiation time under 0.5–2.0 sun irradiation. e) The measured water mass change with 3D PPSDs versus time under 0.5–2.0 sun irradiation. f) Comparison of evaporation rate (E.R.) of 2D (black spheres) and 3D PPSDs (red spheres), and enhanced factors versus solar concentrations. g) The solar-to-thermal conversion efficiency (η) of 2D and 3D PPSDs in this work versus solar concentration compared with values reported in previous literatures on natural, low-cost materials.

Similarly, the E.R. of PPSDs with different thickness also demonstrated an analogous parabola-like trend as T_{eq} under one sun. If the PPSDs layer is too thin, its solar absorption will decrease because of the existence of holes in the PPSDs layer (Fig. S13). If the PPSDs layer is too thick, it will absorb too much water, resulting in unnecessary heat conduction inside the PPSDs layer, thereby reducing the overall efficiency of the solar evaporation system [31]. As a consequent, the PPSDs-3 exhibited the maximum E.R. of 1.21 kg m^{-2} h^{-1} **(**Fig. 3e **and Section S5)**. To vertify this prediction, we built a heat loss model (detailed explanations were stated in **Section S5**, and the heat loss model of PPSDs-3 was illustrated in Fig. 3f) to analyze the thermal environment and heat transfer mechanism. First of all, the solar absorption of PPSDs determined the input of heat for solar evaporation system. Then the absorbed heat can be transported in following ways: 1) evaporation, 2) radiative (Φ) and 3) convective (Q_{conv}) heat loss to the ambient environment and 4) conductive heat loss to the water contained in the PPSDs (Q_{cond1}) and underlying (Q_{cond2}). According to energy conversion principle, the solar-to-thermal efficiency (η) can be expressed as follows:

$$\eta = \alpha - \frac{\Phi}{q_{solar}} - \frac{Q_{conv}}{q_{solar}} - \frac{Q_{cond1}}{q_{solar}} - \frac{Q_{cond2}}{q_{solar}} \tag{1}$$

, where α is the total solar absorption of PPSDs. The theoretical results calculated from heat loss model has the same trend as experimental results of solar-to-thermal conversion efficiency (η) (detailed discussion in **Section S5**), showing that the efficiency of the PPSDs initially increased and then decreased with the increasing thickness, and the best experimental performance was achieved for 3 mm with a solar-to-thermal efficiency of 81% (Fig. 3g).

The photothermal evaporation performance under various illumination intensities (0.5–2.0 sun) was evaluated to further explore the adaptability and sustainability of the solar absorber consisting of PPSDs. The thickness of 3 mm was chosen in following experiments because of the best evaporation performance. As shown in Fig. 4a, the top surface temperatures of PPSDs-3 quickly rose to T_{eq} when light on for 5 min, but the temperature drastically decreased when light off, demonstrating the fast-response photothermal property of PPSDs. IR images of equilibrated PPSDs-3 under 0.5–2.0 sun were illustrated in Fig. 4b. It is noted that localized heat confinement is also critical to achieve high-efficiency solar evaporation [32]. And thus, the actual vertical temperature distribution under one sun irradiation was also investigated. Compared with uniform temperature distribution of pure water, PPSDs-3 strongly illustrated that the heat was strictly confined on the surface of PPSDs, and underlying parts of the evaporation system were not heated up (Fig. 4c and d). Resultantly, a continuous and stable water evaporation could be readily achieved (Fig. 4e). The evaporation rates under different illuminations of 0.5, 1.0, 1.5 and 2.0 suns were 0.61, 1.21, 1.82, and 2.34 kg m^{-2} h^{-1}, respectively, in which a maximum evaporation efficiency of 82.63% under 1.5 sun is realized (Fig. 4f).

The cycles of evaporation performance of PPSDs-3 under a series of solar concentration were measured as shown in Fig. 4g, in which the water evaporation rate after 15 cycles remained almost identical as the previous cycle under one sun. Furthermore, the evaporation durability

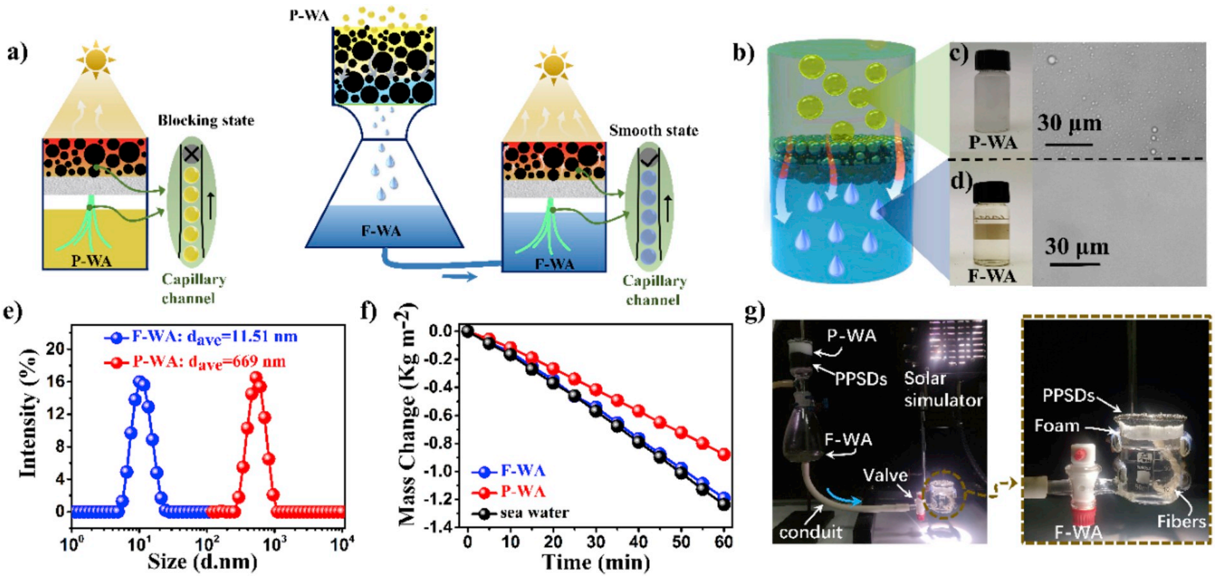

Fig. 6. a) A consecutive progress of oil-water separation and solar evaporation to deal with polluted seawater (P-WA) for a high-efficiency freshwater collection. If P-WA was directly fed into the evaporator, some organics will block the capillary channels, which causes performance degradation. To address above issue, PPSDs were directly applied to remove organics in P-WA to produce filtrated water (F-WA), which then was transferred to evaporator for solar-driven evaporation. b) The PPSD aggregate was utilized for oil-water separation. c) Optical images of polluted water P-WA. d) Optical images of F-WA. e) Dynamic light scattering diameter analysis of P-WA and F-WA. f) Comparison of evaporation performance before and after separation (the blue one is F-WA and the red one is P-WA), showing a significant improvement after separation. g) The home-made continuous setup for oil-water separation and solar evaporation.

of PPSDs-3 was also considered in Fig. 4h, demonstrating almost constant evaporation performance in seven days. The aforementioned results all demonstrated that PPSDs had significant potentials in water purification under long-term solar irradiation. Moreover, the PPSDs still displayed a stable evaporation performance in some harsh environments such as a high-salt environment or an acidic condition (Fig. S14). As shown in Fig. S15, the PPSDs can still maintain a stable state and represent a black color even under H_2SO_4 solution for 1 year. Furthermore, the Raman spectra was also conducted to investigate the difference of chemical components before and after H_2SO_4 immersion. It can be found that there is no remarkable change of characteristic peaks of PPSDs. To evaluate the ability of desalination, concentrations of primary ions in water samples before and after desalination with PPSDs-3 were conducted by ICP-AES. Note that the residual concentration of six primary ions (Na^+, K^+, Mg^{2+}, Ca^{2+}, $Sr^{2+}$and B^{3+}) are far below the concentrations defined by drinking water standard of World Health Organization (WHO) (Fig. 4i).

The preparation of 3D-structure solar evaporator is one of the effective means to enhance the evaporation performance, owing to less heat loss and expanding evaporation area of 3D evaporator than 2D one with the same projected area [33–36]. Herein, a 3D cone structure was selected only as a representative proof to demonstrate that an elevation in water evaporation was achieved by a transformation from 2D to 3D structure. Different from 2D one with the same area, the effective evaporation area of 3D PPSDs was much larger than its projected area. However, for conventional photothermal materials, the preparation of 3D structures requires a tedious process. Drawn inspiration from the sand sculptures on the beach (Fig. S16), a 3D structure of PPSD aggregate was fabricated to enlarge the effective evaporation area under the same projected area, as shown in Fig. 5b. The temperature of 3D PPSDs were also taken under various solar concentration, in which the 3D PPSDs still showed a fast-response photothermal effect (Fig. 5c and d). It should be pointed out that the T_{eq} of 3D PPSDs could reach was lower than that of 2D one at the same irradiation condition, which could minimize heat loss to the ambient environment to enhance evaporation performance (Fig. S17) [33,34]. Consequently, the 3D evaporator can have a positive increase of evaporation rate with 0.73, 1.43, 2.25, and 2.89 kg m^{-2} h^{-1} under different solar intensity of 0.5, 1.0, 1.5, and 2.0 sun, respectively (Fig. 5e). To illustrate the difference of evaporation performance between 2D and 3D PPSDs, an enhancement factors were calculated and plotted versus the optical concentration (Fig. 5f). The result manifested a steady improvement of 3D structure compared with 2D one. As shown in Fig. 5g, corresponding solar-to-thermal efficiencies (η) of 3D and 2D PPSDs were calculated. The η of 3D PPSDs were 93.81%, 94.96%, 97.67%, and 96.01% under the solar intensity of 0.5, 1.0, 1.5, and 2.0 kw m^{-2} illumination, respectively, which were superior to values reported in previous literatures on naturally derived, low-cost materials [37–43]. Nevertheless, the 3D cone was not the optimized 3D structures, and enhancing factor of 3D structure was determined by following four guidelines: 1) expanding the evaporation area, 2) compensation for the incident angle effect and reducing the diffuse reflection, 3) reducing the heat loss, 4) gaining energy from the surrounding environment [44]. Therefore, the PPSDs aggravate has a giant potential to further improve its purification performance via designing more optimized 3D structure in the future.

In the past years, fuel spills at sea, industrial and domestic-wastewater emission, etc. resulting in numerous polluted water (P-WA), mainly composed of oil-water hybrids, have caused concern [45,46]. As an effective alternative, the solar-driven purifier has been chosen to purify P-WA, however, if the P-WA was directly fed into the evaporator, its performance will show a significant decline, which owes to the fact that organics blocked the capillary channels pumping water [47]. To address above issue, a separation-assisted strategy was proposed to treat P-WA as displayed in Fig. 6a. Due to its characteristic of underwater superoleophobicity (Fig. S18) and inner channels mediated by collective effects, the PPSDs aggregate was directly applied to remove organics in P-WA to produce filtrated water (F-WA) via physisorption (Fig. 6b and S19). Then the resulted F-WA was further transferred to the evaporator for solar-driven clean water production. Note that original hydrophilic sand aggregate is enough to separate the emulsion [24,48]. In our work, we have conducted the control experiment to explore the effect of functionalized polymers on the separation performance. Compared with the original sand aggregate, the PPSDs presents a slight flux decrease. The result illustrates that the achieved PPSD aggregate

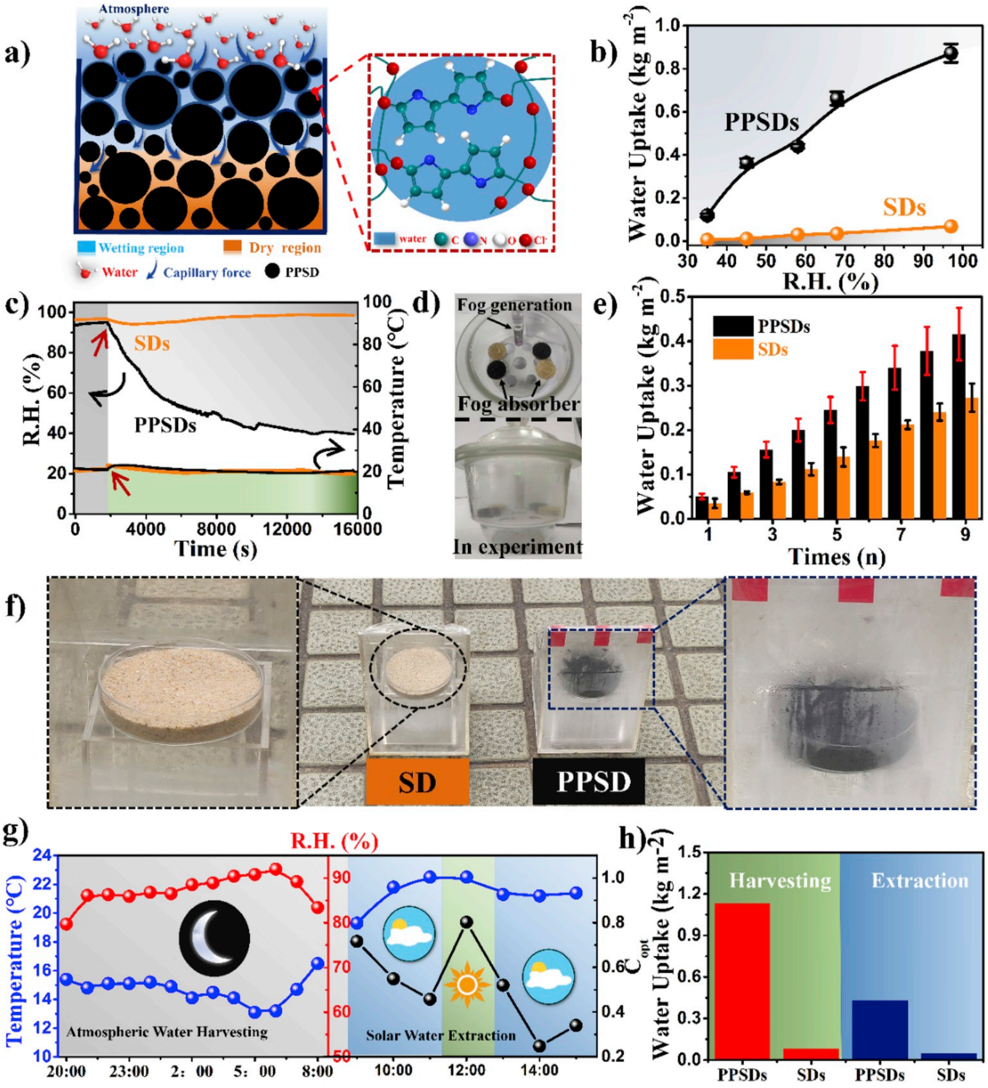

Fig. 7. a) Schematic illustration of the process of atmospheric water harvesting of PPSDs. The water molecules were captured by the PPSDs, and the absorbed water was transferred to the lower layer of PPSDs by capillary force. b) Comparison of the water-uptake ability of PPSDs and SDs at different relative humidity (R.H.) for 12 h. c) R.H. and temperature changes of PPSDs and SDs versus time in a confined sealed container with a volume of ~5600 cm^3. PPSDs and SDs were put into the container at the time indicated by the red arrow. d) Digital photos of experimental setup for fog collection. e) Comparison of the water-uptake ability of PPSDs and SDs in a simulated foggy condition. f) Digital photos of outdoor experiment of atmospheric water harvesting. g) The outdoor environmental conditions (blue spheres refer to temperature, red spheres represent R.H., and black spheres is solar intensity) during experimental procedure. h) Water uptake of PPSDs and SDs after outdoor atmospheric water harvesting.

can also function as an efficient water-oil emulsion separator (Fig. S20). It is obviously found that heterogeneous fed P-WA transformed into colorless clear F-WA after separation with the PPSD aggregate (Fig. 6c and d). In addition, dynamic light scattering diameter analysis was conducted for the evaluation of the quality of F-WA. The results in Fig. 6e revealed that organic droplets (average diameter is 669 nm) in fed P-WA are removed completely and there are only small sizes of colloids below 12 nm in the F-WA after passing through the PPSDs. As a result, the purification performance of the evaporator with F-WA demonstrated a positive improvement than that with P-WA (Fig. 6f), which raised from 0.87 to 1.19 kg m^{-2} h^{-1}. To overcome invalidation of hydrophilic separation materials, the achieved PPSDs aggregate could be effectively reactivated via solar irradiation and washed with ethanol to remove adsorbed organics (Fig. S21). Furthermore, the separation capacity of the resulted PPSDs aggregate could recover even after several cycles (Fig. S22). Next, a home-made continuous prototype for oil-water separation and solar evaporation are presented in Fig. 6g. The left part of the prototypes was for oil-water separation to produce F-WA, which was further transferred to the right magnified part for solar-driven evaporation. Meanwhile, it should be noted that the amount of water source from the separation device was much higher than the evaporation rate enabled by the solar-driven evaporator, which could guarantee high-efficient and sustainable purification (**Section S6**).

In an environment without visible water source, such as the Sahara desert, capturing water from the air is particularly important to relieve the scarcity of fresh water [49]. More recently, it was reported that salt-doped hydrogels or integrated saturated salt solution/aerogel system could both realize an enhanced moisture extraction from the atmosphere [22,23]. Owing to the doping of $FeCl_3$ salt inside the PPy polymers, it was observed that PPSDs could also achieve an effective moisture-trapping from the air (Figs. S23 and S24). In our system, the PPSD aggregate can act as water absorbent, and the captured water molecules can be further released via *in-situ* solar-driven water evaporation. Schematic process of atmospheric water harvesting of PPSDs was illustrated in Fig. 7a, in which the atmospheric moisture was firstly absorbed by upper PPSD aggregate due to the solvation effect of Cl^--doped PPy coating. Subsequently, the absorbed water was transported to underlying PPSDs via the capillary force mediated by inner channels. In order to investigate the capability of water uptake of the resulted PPSDs, we compared pure SDs and PPSDs in various relative humidity (R.H.) for 12 h. Wherein, a huge disparity was also increasing between PPSDs and pure SDs, with the improved R.H.. When the R.H. is 97%, the water uptake of PPSDs reached to 0.87 kg m^{-2} for 12 h, which was 0.81 kg m^{-2} more than that of pure SDs (Fig. 7b). Note that complete desorption of the absorbed water can be effectively achieved under different solar illuminations. As displayed in Fig. S25, a certain amount of water content inside the PPSDs was adopted to investigate the desorption process. When solar intensity with of 0.6, 0.8 and 1.0 kW m^{-2} was conducted, the absorbed water can be mostly released within 2 h, 3 h and 6 h, respectively. The results illustrate that the PPSDs-based absorbent can be effectively recovered.

Furthermore, a comparative experiment of lowering the R.H. between PPSDs and pure SDs in a confined sealed container was also conducted to exhibit their ability of atmospheric water harvesting. From results in Fig. 7c, the R.H. in container with a volume of ~5600 cm^3 could conspicuously decline to 39.6% from ~95% with the presence of PPSDs under a constant temperature for 3.8 h. By contrast, pure SDs could not effectively lower the R.H. in the container at the same condition. As a common weather phenomenon in nature, fog is also absorbed by the resulted PPSDs. To simulate the foggy weather, a nanospray was adopted to produce moisture in a confined sealed container as illustrated in Fig. 7d. In every cycle, first, the duration of fog generation was 1 min, and then fog absorption was lasting for 4 min (Fig. S26). As expected, both PPSDs and pure SDs performed a successive enhancement in water harvesting as the cycle increases in a foggy environment, in which PPSDs had a better yield of 0.42 kg m^{-2} after 9-times cycle, which was 1.52 times than that of pure SD (Fig. 7e). Moreover, the outdoor experiment was conducted to further evaluate the ability of PPSDs to acquire fresh water in a natural environmental condition. After absorbing moisture for 12 h, PPSDs and pure SDs were placed into a sealed collecting device, as shown in Fig. 7f, to release the absorbed water for 6 h under natural solar irradiation. Note that more vaporized water could be obtained in the home-made prototype equipped with PPSDs, illustrated in the magnified images in Fig. 7f. Additionally, the environmental condition of outdoor experiment was revealed in Fig. 7g. As a result, the yield of PPSDs in outdoor atmospheric water harvesting was up to 1.13 kg m^{-2}, which was more than that of SDs (Fig. 7h, red columns). Surprisingly, the value obtained in outdoor experiment was higher than that of sealed container in lab, which is probably because the air flow could accelerate moisture absorption in outdoor open environment. Finally, the output of water extraction for PPSDs can reach to ~0.43 kg m^{-2}, much higher than that of pure SD (~0.05 kg m^{-2}), under natural solar irradiation of 6 h on a cloudy day (Fig. 7h, blue columns).

3. Conclusion

To conclude, as a cost-effective, scalable and functional platform, the natural sand particles are rationally decorated to realize multifunctional black sand aggregate, which can adapt to diverse environments to collect purified water under sunlight illumination. In our system, the sand particles were successively modified with PDA binder and photothermal PPy polymers to achieve desired solar-to-thermal conversion, and the fabrication process of PPSD was conducted through a wet-method in mild condition, which is accessible to factories and easy to scale up. Furthermore, the collective behaviors of the particles can further endow the resulted PPSDs aggregate with desirable pores in micro scale, in which the functions of water pumping and water storage can be effectively realized. As a result, PPSDs can directly be utilized to realize an efficient solar-to-thermal conversion for interfacial water evaporation with the rate of 1.21 kg m^{-2} h^{-1}. Furthermore, the configurable 3D geometry of PPSDs can be readily designed for an enhanced evaporation rate of 1.43 kg m^{-2} h^{-1}, which is superior than pervious most reports on naturally derived materials. Significantly, the achieved PPSDs can also function as a pre-handling separator to treat the oil-water emulsion contamination from cities and industrial areas and further realize a stable localized solar heating with a remarkable improvement of evaporation rate the from 0.87 to 1.19 kg m^{-2} h^{-1}. More interestingly, the introduction of Cl^- has endowed PPSDs with the desirable capability of moisture absorption. In some droughty areas or deserts, PPSDs can effectively harvest atmospheric moisture and further release them by *in situ* solar-driven evaporation for clean water collection. In actual outdoor experiments of atmospheric water harvesting, PPSDs demonstrated a clean water collecting ability of ~1.13 kg m^{-2}, much higher than that of pure SD (~0.07 kg m^{-2}). Therefore, the collective multifunctional PPSD aggregate has realized an environmental-adaptive purified water collection in changeable circumstance.

Declaration of competing interest

The authors declare no competing financial interest.

Acknowledgments

We thank the Natural Science Foundation of China (51803226, 51573203), Key Research Program of Frontier Sciences, Chinese Academy of Sciences (QYZDB-SSW-SLH036), Postdoctoral Innovation Talent Support Program (BX20180321), China Postdoctoral Science Foundation (2018M630695) and Ningbo Science and Technology Bureau (2018A610108).

Appendix A. Supplementary data

Supplementary data to this article can be found online at https://doi.org/10.1016/j.nanoen.2019.104311.

References

[1] E.G.R.S. Davies, P. Slobodan, Adv. Water Resour. 34 (2011) 684.
[2] J.H.D. Pimentel, E. Preiss, O. White, H. Fang, L. Mesnick, T. Barsky, S. Tariche, J. Schreck, S. Alpert, Bioscience 47 (1997) 97.
[3] G. Rasul, Environ. Sci. Policy 39 (2014) 35.
[4] M.A. Palmer, Nature 467 (2010) 534.
[5] M. Elimelech, W.A. Phillip, Science 333 (2011) 712.
[6] P. Zhang, Q. Liao, H. Yao, Y. Huang, H. Cheng, L.T. Qu, Energy Storage Mater. 18 (2019) 429.
[7] L. Zhu, M. Gao, C.K.N. Peh, G.W. Ho, Nano Energy 57 (2019) 507.
[8] P. Tao, G. Ni, C.Y. Song, W. Shang, J.B. Wu, J. Zhu, G. Chen, T. Deng, Nat. Energy 3 (2018) 1031.
[9] L.L. Zhu, M.M. Gao, C.K.N. Peh, G.W. Ho, Mater. Horiz. 5 (2018) 323.
[10] C. Chen, Y. Kuang, L.B. Hu, Joule, vol. 3, 2019, p. 1.
[11] P. Xiao, J. He, Y. Liang, C. Zhang, J. Gu, J. Zhang, Y. Huang, Sh Kuo, T. Chen, Solar RRL 3 (2019) 1900004.
[12] F. Zhao, X. Zhou, Y. Shi, X. Qian, M. Alexander, X. Zhao, S. Mendez, R. Yang, L. Qu, G.H. Yu, Nat. Nanotechnol. 13 (2018) 489.
[13] F.Z.X.Y. Zhou, Y.H. Guo, B. Rosenberger, G.H. Yu, Sci. Adv. 5 (2019), eaaw5484.
[14] J.L.L.N. Xu, Y. Wang, C. Fang, X.Q. Li, Y.X. Wang, L. Zhou, B. Zhu, Z. Wu, S.N. Zhu, J. Zhu, Sci. Adv. 5 (2019) eaaw7013.
[15] T. Gao, Y. Li, C. Chen, Z. Yang, Y. Kuang, C. Jia, J. Song, M.H. Emily, B. Liu, H. Huang, J. Yu, B. Yang, L.B. Hu, Small Methods (2018) 1800176.
[16] Y. Kuang, C. Chen, S. He, E.M. Hitz, Y. Wang, W. Gan, R. Mi, L. Hu, Adv. Mater. (2019), e1900498.
[17] L.L. Zhu, M.M. Gao, C.K.N. Peh, X.Q. Wang, G.W. Ho, Adv. Energy Mater. (2018) 1702149.
[18] L.L. Zhu, T.P. Ding, M.M. Gao, C.K.N. Peh, G.W. Ho, Adv. Energy Mater. (2019) 1900250.
[19] M. Gao, C.K. Peh, H.T. Phan, L. Zhu, G.W. Ho, Adv. Energy Mater. 8 (2018) 1800711.
[20] C. Chen, L. Zhou, J. Yu, Y. Wang, S. Nie, S. Zhu, J. Zhu, Nano Energy 51 (2018) 451.
[21] M.Q. Yang, M. Gao, M. Hong, G.W. Ho, Adv. Mater. 30 (2018), e1802894.
[22] F. Zhao, X.Y. Zhou, Y. Liu, Y. Shi, Y.F. Dai, G.H. Yu, Adv. Mater. (2019) 1806446.
[23] X. Wang, X. Li, G. Liu, J. Li, X. Hu, N. Xu, W. Zhao, B. Zhu, J. Zhu, Angew. Chem. Int. Ed. 58 (2019) 12054.
[24] J. Li, C. Xu, C. Guo, H. Tian, F. Zha, L. Guo, J. Mater. Chem. 6 (2018) 223.
[25] V.K. Thakur, D. Vennerberg, M.R. Kessler, ACS Appl. Mater. Interfaces 6 (2014) 9349.
[26] Q. Lin, Y. Yang, Y. Ma, R. Zhang, J. Wang, X. Chen, Z.Z. Shao, Nano Lett. 18 (2018) 7485.
[27] Y. Wang, F. Gu, L. Ni, K. Liang, K. Marcus, S. Liu, F. Yang, J. Chen, Z.S. Feng, Nanoscale 9 (2017) 18318.
[28] S. Wan, S. Fang, L. Jiang, Q. Cheng, R.H. Baughman, Adv. Mater. (2018) 1802733.
[29] Y. Wang, C. Wang, X. Song, M. Huang, S.K. Megarajan, S.F. Shaukat, H.Q. Jiang, J. Mater. Chem. 6 (2018) 9874.
[30] R.Y. Li, L.B. Zhang, L. Shi, P. Wang, ACS Nano 11 (2017) 3752.
[31] X.Y. Yin, Y. Zhang, Q.Q. Guo, X.B. Cai, Z.F. Ding, J. Yang, ACS Appl. Mater. Interfaces 10 (2018) 10998.
[32] Q.S. Jiang, L.M. Tian, K.K. Liu, S. Tadepalli, R. Raliya, P. Biswas, R.R. Naik, S. Singamaneni, Adv. Mater. 28 (2016) 9400.
[33] F. Ni, P. Xiao, C. Zhang, Y. Liang, J.C. Gu, L. Zhang, T. Chen, ACS Appl. Mater. Interfaces 11 (2019) 15498–15506.

[34] H. Song, Y. Liu, Z. Liu, M.H. Singer, C. Li, A.R. Cheney, D. Ji, L. Zhou, N. Zhang, X. Zeng, Z. Bei, Z. Yu, S. Jiang, Q. Gan, Adv. Sci. 5 (2018) 1800222.
[35] X. Li, R. Lin, G. Ni, N. Xu, X. Hu, B. Zhu, G. Lv, J. Li, S. Zhu, J. Zhu, Natl. Sci. Rev. 5 (2018) 70.
[36] P. Xiao, J. Gu, C. Zhang, F. Ni, Y. Liang, J. He, L. Zhang, J. Ouyang, S.-W. Kuo, T. Chen, Nano Energy 60 (2019) 841.
[37] T. Li, H. Liu, X.P. Zhao, G. Chen, J.Q. Dai, G. Pastel, C. Jia, C.J. Chen, E. Hitz, D. Siddhartha, R.G. Yang, L.B. Hu, Adv. Funct. Mater. 28 (2018) 1707134.
[38] M.W. Zhu, Y.J. Li, F.J. Chen, X.Y. Zhu, J.Q. Dai, Y.F. Li, Z. Yang, X.J. Yan, J. W. Song, Y.B. Wang, E. Hitz, W. Luo, M.H. Lu, B. Yang, L.B. Hu, Adv. Energy Mater. 8 (2018) 1701028.
[39] M. Zhu, J. Yu, C. Ma, C. Zhang, D. Wu, H.T. Zhu, Sol. Energy Mater. Sol. Cells 191 (2019) 83.
[40] J.L. Fang, J. Gu, Q. Liu, W. Zhang, H. Su, D. Zhang, Chem. Mater. 30 (2018) 6217.
[41] N. Xu, X.Z. Hu, W.C. Xu, X.Q. Li, L. Zhou, S.N. Zhu, J. Zhu, Adv. Mater. 29 (2017) 1606762.
[42] Y. Bian, Q. Du, K. Tang, Y. Shen, L. Hao, D. Zhou, X. Wang, Z. Xu, H. Zhang, L. J. Zhao, S.M. Zhu, J.D. Ye, H. Lu, Y. Yang, R. Zhang, Y.D. Zheng, S.L. Gu, Adv. Mater. Technol. (2018) 1800593.
[43] C.B. Wang, Z.T. Li, T. Lei, H.L. Ma, J.B. Su, S. Ling, W. Wang, Adv. Sustain. Syst. (2019) 1800144.
[44] J. Zhou, Y. Gu, P. Liu, P. Wang, L. Miao, J. Liu, A. Wei, X. Mu, J. Li, J. Zhu, Adv. Funct. Mater. (2019) 1903255.
[45] Z. Xu, Y. Zhao, H. Wang, X. Wang, T. Lin, Angew. Chem. Int. Ed. 54 (2015) 4527.
[46] M.A. Shannon, P.W. Bohn, M. Elimelech, J.G. Georgiadis, B.J. Marinas, A. M. Mayes, Nature 452 (2008) 301.
[47] T. Li, Q. Fang, X. Xi, Y. Chen, F. Liu, J. Mater. Chem. 7 (2018) 586.
[48] J. Yong, F. Chen, Q. Yang, H. Bian, G. Du, C. Shan, J. Huo, Y. Fang, X. Hou, Adv. Mater. Inter. 3 (2016) 1500650.
[49] A.R. Parker, Chris R. Lawrence, Nature 414 (2001) 33.